
Advancements in Near-Field Antenna Characterization: A Compressive Sensing Perspective

M. Salucci, N. Anselmi, and A. Massa

2024/03/22

Contents

1	Test Case 2: <i>AUT</i> with a magnitude failure and phase shift affecting a single row; incremented failure ranges to build the over-complete basis ($\nu^{(s)} \in [0.0, 1.0]$, $F^{(s)} = 7$ and $\gamma^{(s)} \in [-\pi, \pi]$, $P^{(s)} = 5$)	3
1.1	Failures of the <i>AUT</i> 3 rd row ($\nu^{(3)} = 0.45$, $\gamma^{(3)} = \frac{\pi}{3}$)	3
1.1.1	Comparison between original (<i>OMP</i>) and alternative (<i>BCS</i>) MbD	7
1.1.2	<i>OMP</i> vs best <i>BCS</i>	12
1.2	Failures of the <i>AUT</i> 9 th row ($\nu^{(9)} = 0.45$, $\gamma^{(9)} = \frac{\pi}{3}$)	17
1.2.1	Comparison between original (<i>OMP</i>) and alternative (<i>BCS</i>) MbD	17
1.2.2	<i>OMP</i> vs best <i>BCS</i>	22

1 Test Case 2: AUT with a magnitude failure and phase shift affecting a single row; incremented failure ranges to build the over-complete basis ($\nu^{(s)} \in [0.0, 1.0]$), $F^{(s)} = 7$ and $\gamma^{(s)} \in [-\pi, \pi]$, $P^{(s)} = 5$)

1.1 Failures of the AUT 3rd row ($\nu^{(3)} = 0.45$, $\gamma^{(3)} = \frac{\pi}{3}$)

Parameters

Gold Antenna (Without Defects)

- Geometry : Planar array of microstrip patches on the (x, y) plane;
- Working Frequency : $f = 3.6 [GHz]$ ($\lambda = 83.27 \times 10^{-3} [m]$ in free space);
- Substrate (PEC-backed) :
 - Dimensions : infinite;
 - Relative Permittivity : $\epsilon_{r,sub} = 4.7$;
 - Loss Tangent : $\tan \delta_{sub} = 0.014$;
 - Thickness : $h_{sub} = 0.019 [\lambda]$ ($1.6 [mm]$);
- Microstrip patches :
 - Dimensions : $l_x \approx 0.22 [\lambda]$ ($18.16 [mm]$), $l_y \approx 0.33 [\lambda]$ ($27.25 [mm]$);
 - Feeding : pin-fed;
- Spacing between elements : $d_x = d_y = \frac{\lambda}{2}$;
- Number of elements in each row : $N_x = 6$;
- Number of elements in each column : $N_y = 10$;
- Total number of elements : $N = (N_x \times N_y) = 60$;
- Total size of the antenna : $L_x = 5 [\lambda]$, $L_y = 9 [\lambda]$;
- Element excitations : $w_n^{(s)} = 1.0 + j0.0$, $n = 1, \dots, N^{(s)}$, $s = 1, \dots, S$;

Antenna Under Test (AUT - With Defects)

1. Failures of the excitation magnitude of the 3rd row;
 - Failure factor of the elements in the 3rd row ($s = 3$) : $\nu^{(3)} = 0.45$;
2. Failures of the excitation phase of the 3rd row;

- Phase shift of the elements in the 3rd row ($s = 3$) : $\gamma^{(3)} = \frac{\pi}{3} [rad]$;

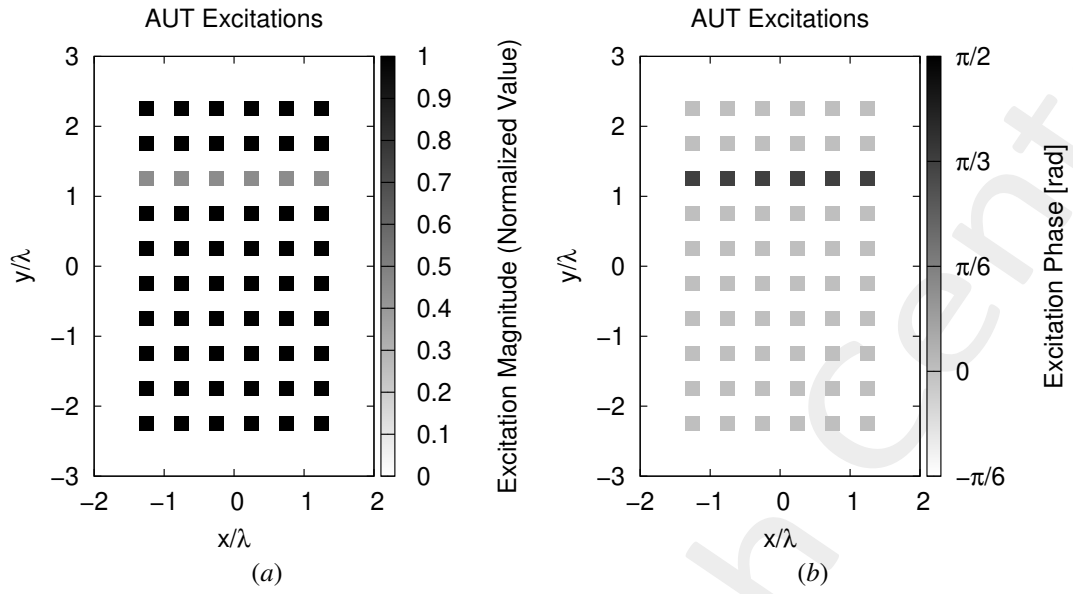


Figure 1: (a) Magnitude of the element excitations in the AUT ($\nu^{(3)} = 0.45$), (b) phase of the element excitations in the AUT ($\gamma^{(3)} = \frac{\pi}{3} [rad]$).

Measurement Set-Up

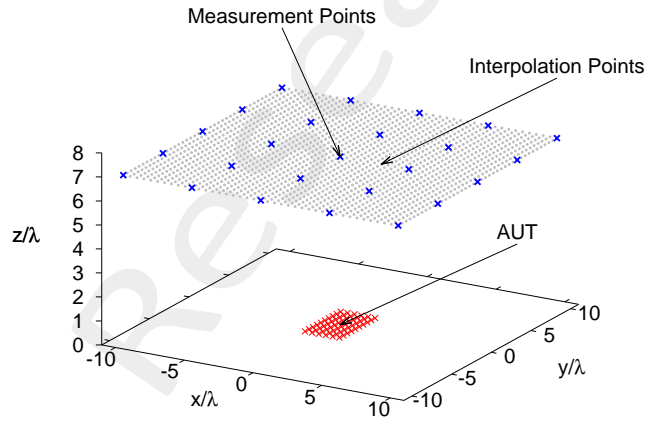


Figure 2: Disposition of the interpolation points ($T = 1681$) and of the measurement points ($M = 25$) in the near-field region of the AUT

- Type of measurements : near-field;
- Height of the measurement region : $H = 7 [\lambda]$;
- Interpolation points :
 - Number of points : $T = 41 \times 41 = 1681$;
 - Coordinates : $x_t \in [-10, 10] [\lambda]$, $y_t \in [-10, 10] [\lambda]$, $z_t = H [\lambda]$, $t = 1, \dots, T$;
 - Interpolation step : $\Delta_{x/y}^{int} = 0.5 [\lambda]$;
- Measurement points :

- Coordinates : $x_m^{meas} \in [-10, 10] [\lambda]$, $y_m^{meas} \in [-10, 10] [\lambda]$, $z_m^{meas} = H [\lambda]$, $m = 1, \dots, M$;
- Number of points : $M_{x/y} = 5 \rightarrow M = 25$;
- Measurement step : $\Delta_{x/y}^{meas} = 5 [\lambda]$
- Ratio between number of measurements and total number of elements : $(M/N) = 0.42$;

Measurement-by-Design Technique

- Number of generated bases : $B = 20$;
- Bases $b = 1, \dots, 10$: magnitude failures in each row ($s = 1, \dots, 10$)
 - **Failure factor of the elements** : $\nu^{(s)} \in [0.0, 1.0]$, $s = 1, \dots, 10$;
 - Number of simulated failure factors : $F^{(s)} = 7$, $s = 1, \dots, 10$;
- Bases $b = 11, \dots, 20$: phase failures in each row ($s = 1, \dots, 10$)
 - **Phase shift of the elements** : $\gamma^{(s)} \in [-\pi, \pi] [rad]$, $s = 1, \dots, 10$;
 - Number of simulated phase shifts: $P^{(s)} = 5$, $s = 1, \dots, 10$;
- Threshold on the singular values magnitude (normalized) : $\eta = -40 [dB]$;
- Total number of simulated *AUT* configurations : $K = S \times (F^{(s)} + P^{(s)}) = 10 \times (7 + 5) = 120$;

Dimension of the Over-Complete Basis

The dimension of the over-complete basis is

$$Q = 40$$

This number is given by the sum of the vectors belonging to the two considered bases:

1. Magnitude failures : $Q_1, \dots, Q_{10} = 2$;
2. Phase failures : $Q_{11}, \dots, Q_{20} = 2$.

Alternative (BCS) MbD parameters

- Toleration factor for *BCS* solver: $Tolerance = 1 \times 10^{-8}$;
- Initial noise variance for *BCS* solver: $\eta_0^{opt1} = 10^{-2}$ and $\eta_0^{opt2} = 5 \times 10^{-4}$. This values have been obtained as a result of a calibration procedure;

Original (OMP) MbD parameters

- Max. number of iterations of the *OMP* algorithm : $I = \{1; 2; 3; \dots; 10\}$;

- Selected iteration to report the results: $I = 6$; this choice is justified by the fact that at this iteration the *OMP* algorithm reaches the best near field error as shown in the following Fig. 3.

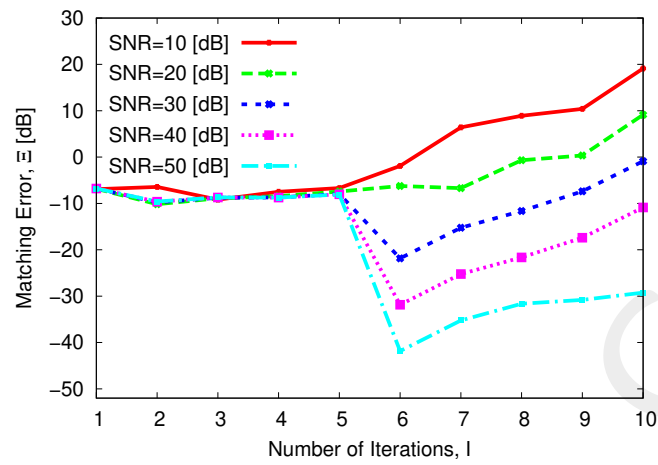


Figure 3: Behaviour of the near-field matching error versus the number of *OMP* iterations, I .

Noise

- SNR on the measured data : $SNR = \{50; 40; 30; 20; 10\} [dB]$;
- Noise seed : $Noise_Seed = 11$.

1.1.1 Comparison between original (*OMP*) and alternative (*BCS*) MbD

Near-Field Error

The comparison, in terms of near field error, between the original (*OMP*) and the alternative (*BCS*) MbD is reported in the following Fig. 4.

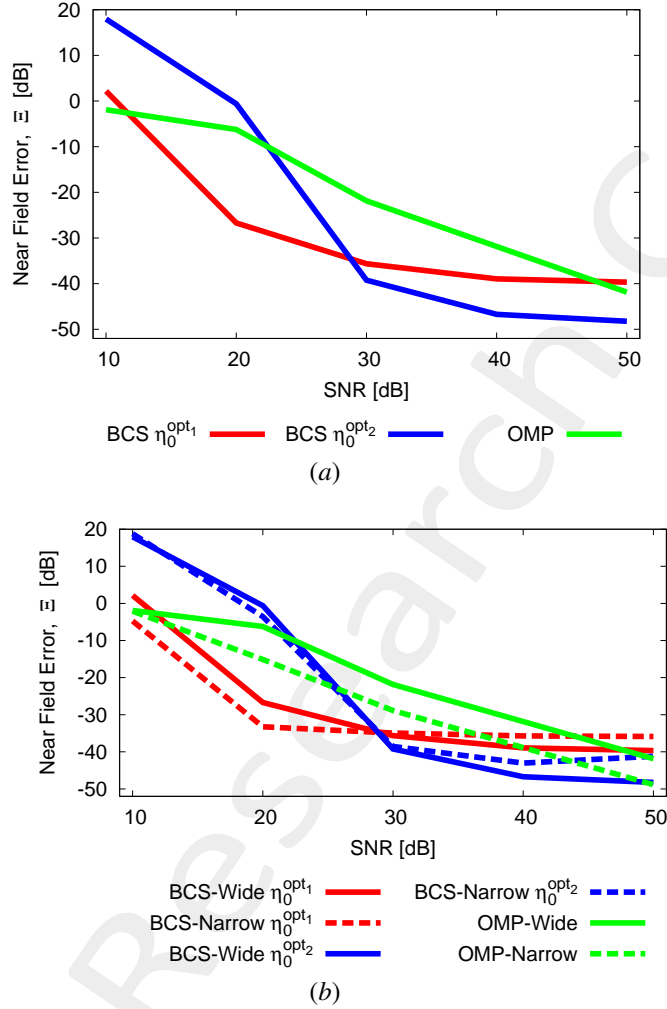


Figure 4: (a) Near Field Error comparison between original (*OMP*) and alternative (*BCS*) MbD for different *SNR* values and (b) comparison between the results

<i>SNR</i> [dB]	Near Field Error, Ξ [dB]		
	<i>BCS</i>		<i>OMP</i>
	η_0^{opt1}	η_0^{opt2}	
50	-39.67	-48.24	-41.85
40	-38.95	-46.72	-31.85
30	-35.54	-39.24	-21.85
20	-26.70	-0.61	-6.23
10	2.16	17.96	-1.90

Table I: Near Field Errors obtained by the original (*OMP*) and alternative (*BCS*) MbD

Observations

Considering Fig. 4 (a) :

-
- The *OMP* algorithm performs poorly until $SNR = 30 [dB]$ from which starts to obtain an error $\Xi < -20 [dB]$ which linearly decreases as the SNR value increases; nevertheless, among the used solvers and in the considered test case, it is possible to evaluate the *OMP* as the algorithm that reaches the worst result;
 - about the *BCS* solver:
 - using η_0^{opt1} , the *BCS* reaches the best results since it outperforms the other algorithm at low SNR values (i.e. $SNR < 30 [dB]$) and presents an error comparable to the others for higher SNR values;
 - using η_0^{opt2} , the *BCS* obtains results that are worse or comparable with the others for $SNR < 30 [dB]$, but for $SNR \geq 30 [dB]$ it achieves better results than the other methods, in particular at $SNR = 30 [dB]$ it presents an error which is more or less $18 [dB]$ lower than that of the *OMP*;

Considering Fig. 4 (b) :

- The increase of the failure ranges considered to build the over-complete basis involves a performance deterioration of the *OMP* algorithm; instead, the *BCS* solver seems to be quite insensitive to this change since the results are essentially the same.

Estimated Near-Field

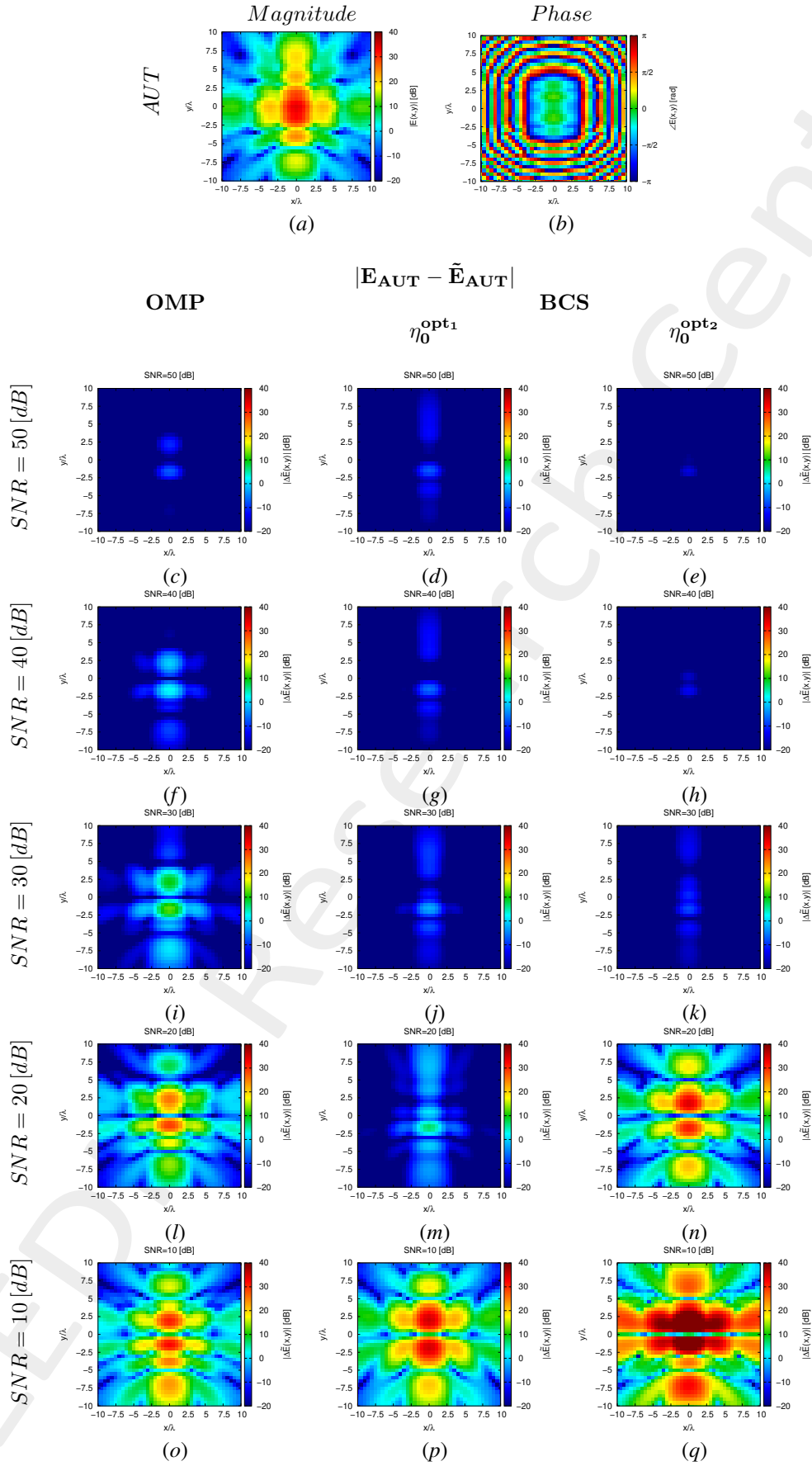


Figure 5: Magnitude difference between the actual and estimated 2 – D near-field pattern when processing noisy measurements at different SNRs.

Estimated Coefficients

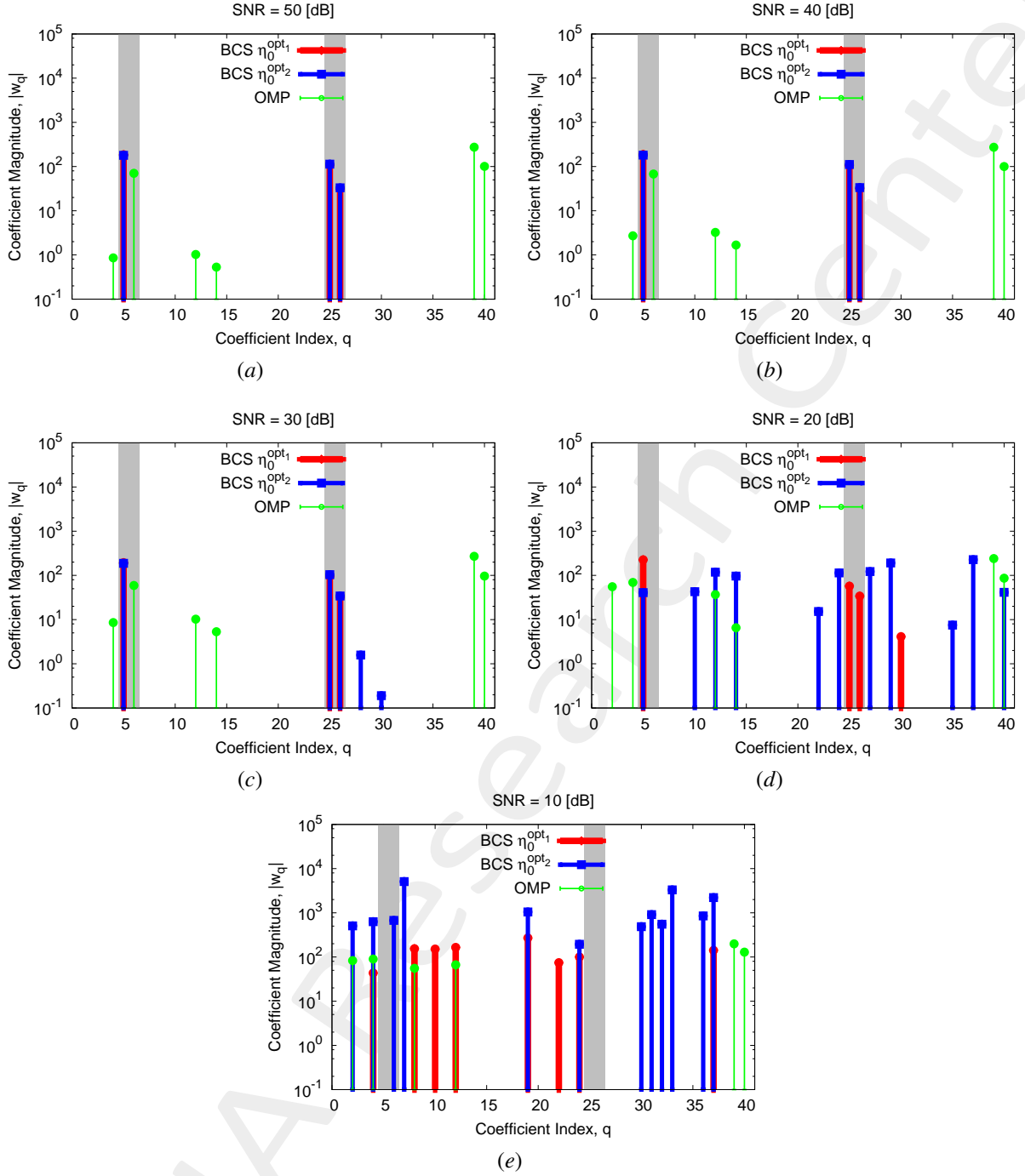


Figure 6: Coefficient comparison between original (*OMP*) and alternative (*BCS*) MbD : (a) $SNR = 50$ [dB], (b) $SNR = 40$ [dB], (c) $SNR = 30$ [dB], (d) $SNR = 20$ [dB], (e) $SNR = 10$ [dB]

Observations

- The *OMP* algorithm is able to select only the vector concerning the magnitude failure affecting the 3^{rd} row of the *AUT* for $SNR \geq 30$ [dB] and none of the vectors associated to the phase failure. Moreover, the *OMP* chooses the same vectors for $SNR \geq 30$ [dB];
- The *BCS* algorithm obtains solutions which are not much sparse when the $SNR \in [10, 20]$, in particular when η_0^{opt2} is used, but become sparse for $SNR \geq 30$ [dB]; furthermore, the *BCS* correctly detects both magnitude and

phase failures, at first with low precision (i.e. for $SNR = 20 [dB]$) and then with very high exactness, especially when η_0^{opt1} is used.

ELEDIA Research Center

1.1.2 OMP vs best BCS

The main idea of this section is to compare the performance of the *OMP* algorithm and the best *BCS* configuration.

Near-Field Error

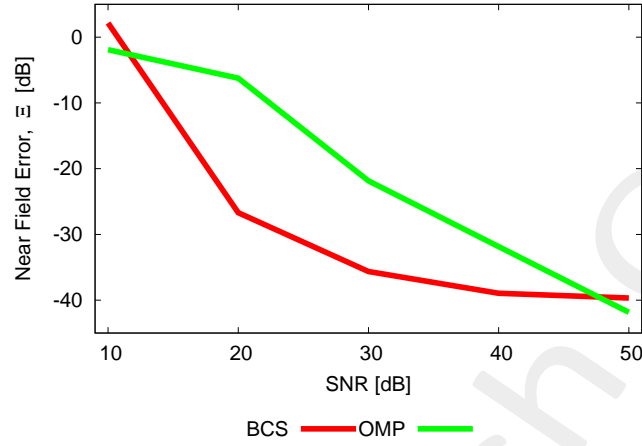


Figure 7: Near Field Error comparison between original (*OMP*) and alternative (*BCS*) MbD for different *SNR* values.

<i>SNR</i> [dB]	Near Field Error, Ξ [dB]	
	<i>BCS</i>	<i>OMP</i>
50	-39.67	-41.85
40	-38.95	-31.85
30	-35.54	-21.85
20	-26.70	-6.23
10	2.16	-1.90

Table II: Near Field Errors obtained by the original (*OMP*) and alternative (*BCS*) MbD

Estimated Far-Field

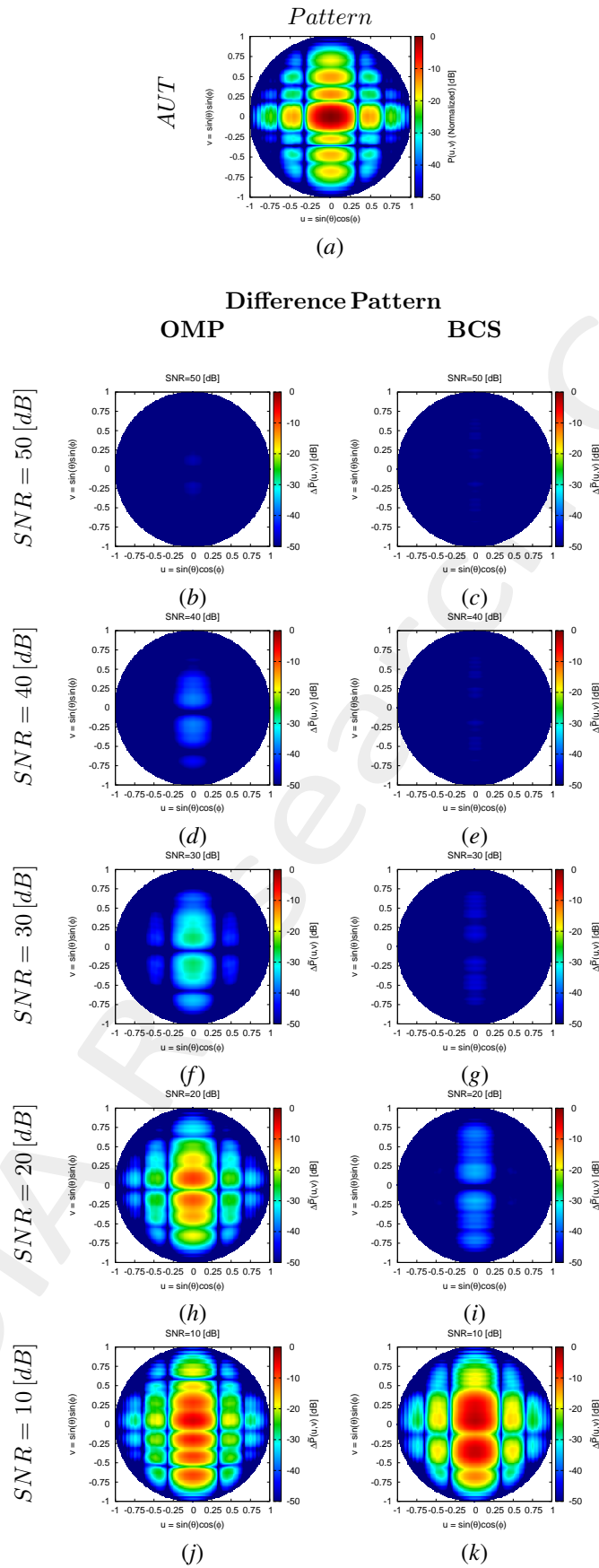


Figure 8: Difference between the actual and estimated 2 – D far-field pattern when processing noisy measurements at different $SNRs$.

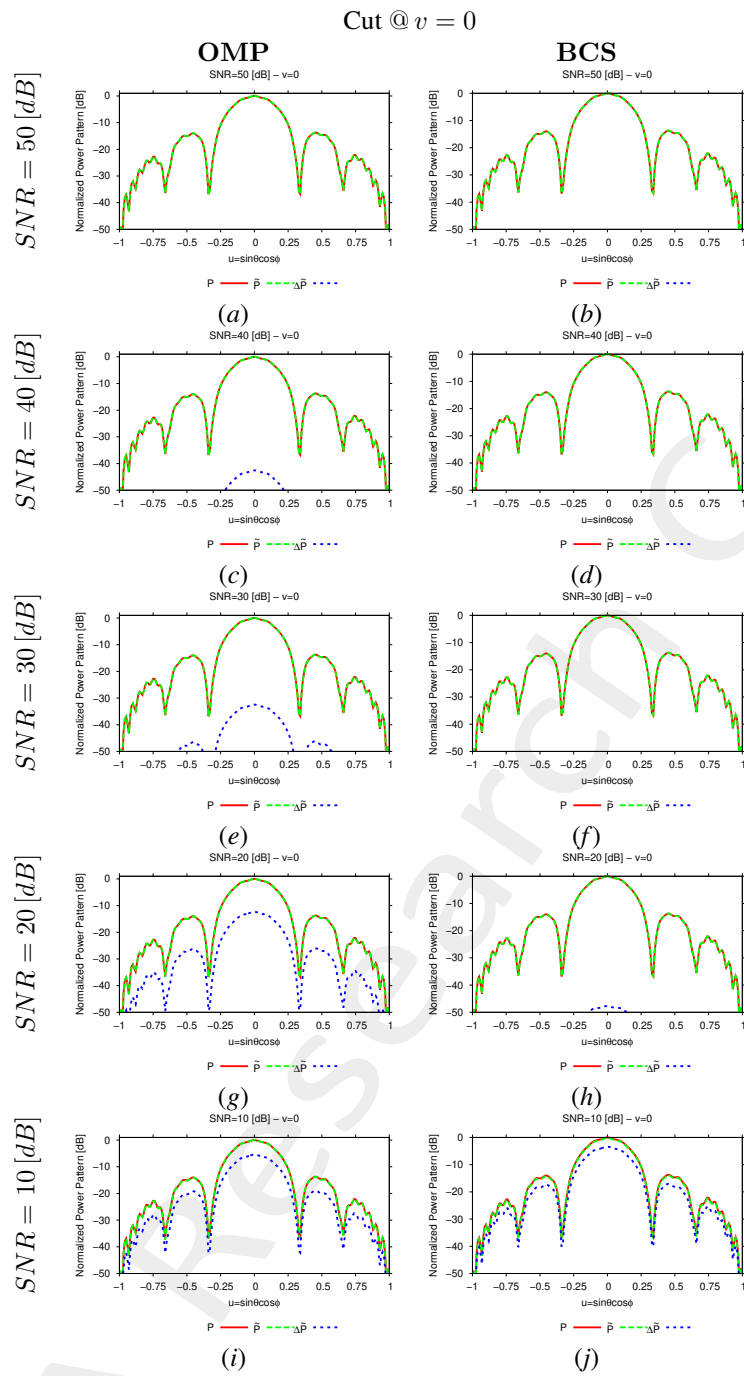


Figure 9: 1-D cuts of the estimated far-field pattern (obtained through near-to-far-field transformation from the estimated near-field patterns) under several noisy conditions

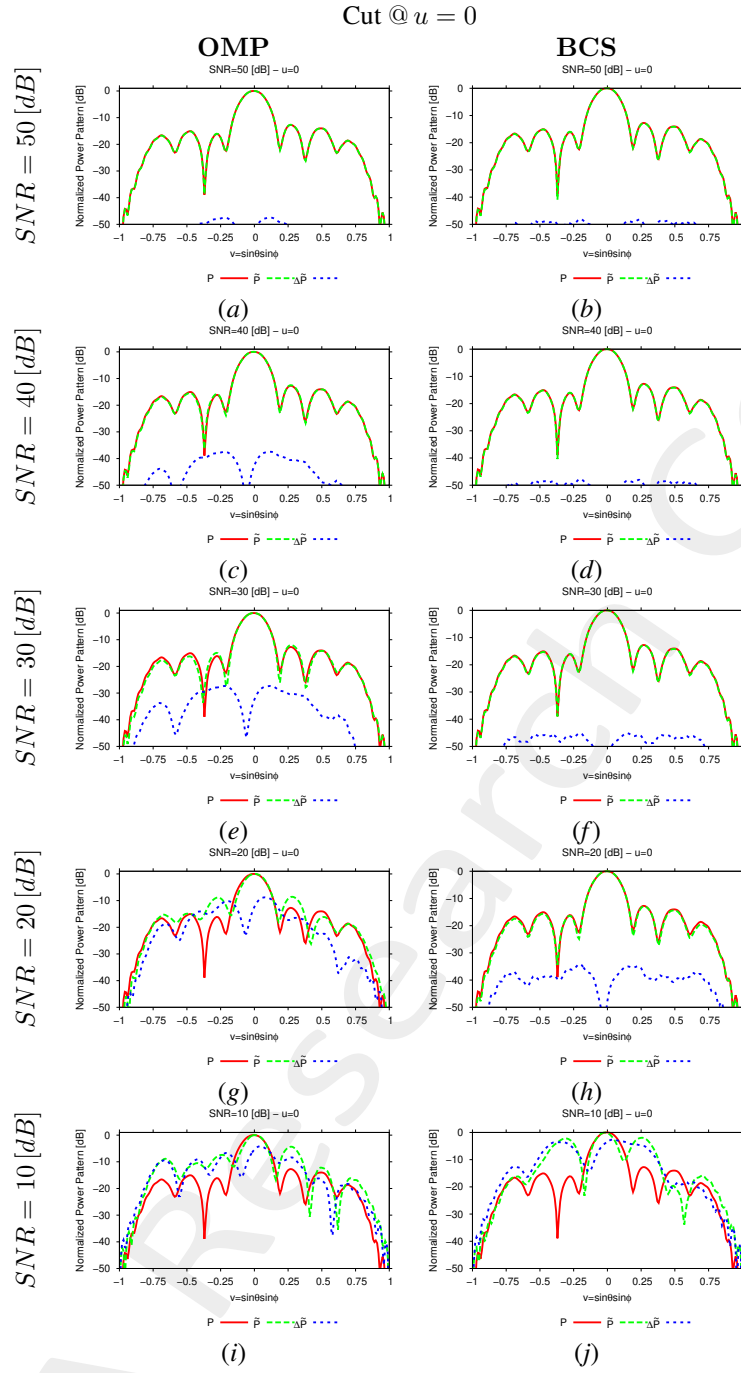


Figure 10: 1 – D cuts of the estimated far-field pattern (obtained through near-to-far-field transformation from the estimated near-field patterns) under several noisy conditions

SNR [dB]	Far – Field Error, χ [dB]	
	BCS	OMP
50	-41.27	-42.80
40	-40.91	-32.77
30	-38.28	-22.65
20	-29.17	-6.15
10	1.59	-1.44

Table III: Far-field matching error between the actual and estimated AUT patterns (both obtained through near-to-far-field transformation from the corresponding near-field patterns) under several noisy conditions.

Estimated Coefficients

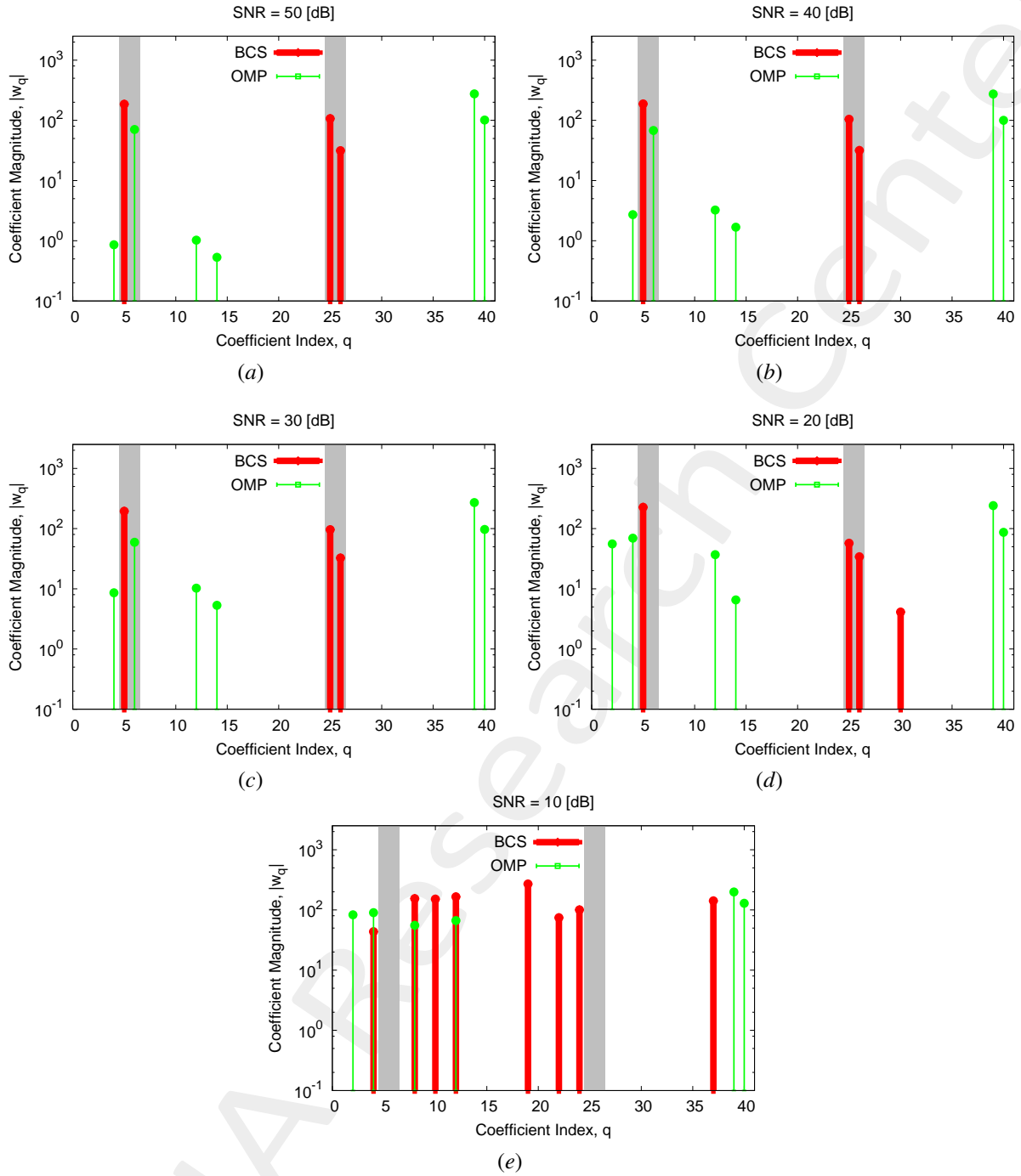


Figure 11: Coefficient comparison between original (*OMP*) and alternative (*BCS*) MbD: (a) $SNR = 50$ [dB], (b) $SNR = 40$ [dB], (c) $SNR = 30$ [dB], (d) $SNR = 20$ [dB], (e) $SNR = 10$ [dB]

1.2 Failures of the AUT 9th row ($\nu^{(9)} = 0.45, \gamma^{(9)} = \frac{\pi}{3}$)

Note: The simulation parameters are the same of those listed in previous section, except for the following ones:

- Index of the failed (subarray) row : $s = 9$;

Original (OMP) MbD parameters

- Max. number of iterations of the OMP algorithm : $I = \{1; 2; 3; \dots; 10\}$;
- Selected iteration to report the results: $I = 10$; this choice is justified by the fact that at this iteration the OMP algorithm reaches the best near field error as shown in the following Fig. 12.

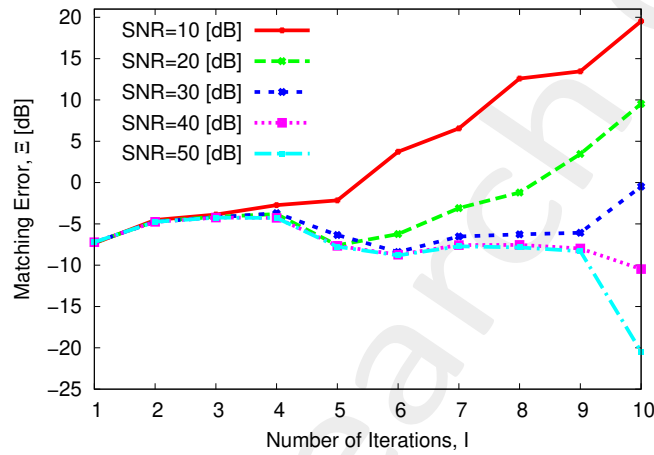


Figure 12: Behaviour of the near-field matching error versus the number of OMP iterations, I .

1.2.1 Comparison between original (OMP) and alternative (BCS) MbD

Near-Field Error

The comparison, in terms of near field error, between the original (OMP) and the alternative (BCS) MbD is reported in the following Fig. 13.

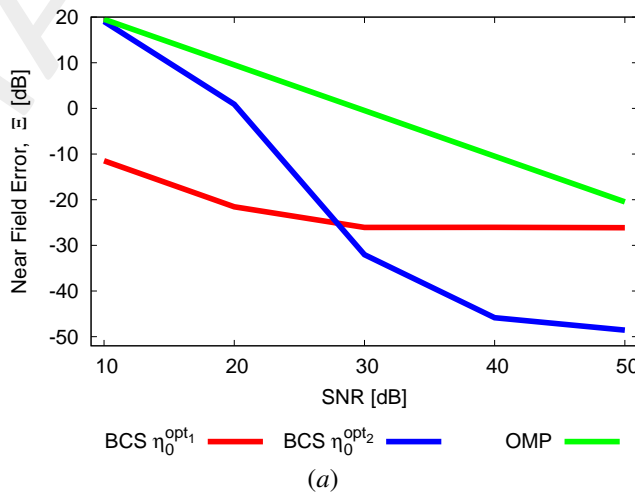


Figure 13: (a) Near Field Error comparison between original (OMP) and alternative (BCS) MbD for different SNR values

$SNR [dB]$	Near Field Error, $\Xi [dB]$		
	BCS		OMP
	η_0^{opt1}	η_0^{opt2}	
50	-26.12	-48.57	-20.47
40	-26.04	-45.85	-10.47
30	-26.07	-32.03	-0.47
20	-21.56	0.89	9.53
10	-11.46	19.04	19.53

Table IV: Near Field Errors obtained by the original (*OMP*) and alternative (*BCS*) MbD

Observations

- The *OMP* algorithm performs poorly whatever the *SNR* value and among the used solvers in the considered test case, it is possible to evaluate the *OMP* as the algorithm that reaches the worst result since it is not able to go below an error $\Xi \simeq 20 [dB]$;
- about the *BCS* solver:
 - using η_0^{opt1} , the *BCS* reaches the best results for low *SNR* values (i.e. $SNR < 30 [dB]$) and presents an error $\Xi \simeq 26 [dB]$ for higher *SNR* values, which is a better result if compared to that of *OMP* solver but not if compared to the other *BCS* version;
 - using η_0^{opt2} , the *BCS* obtains results that are between those of the *OMP* and the other *BCS* for $SNR < 30 [dB]$, but for $SNR \geq 30 [dB]$ it outperforms the other methods, in particular at $SNR \geq 40 [dB]$ it presents an error which is more than $20 [dB]$ lower than the best of the others;

Estimated Near-Field

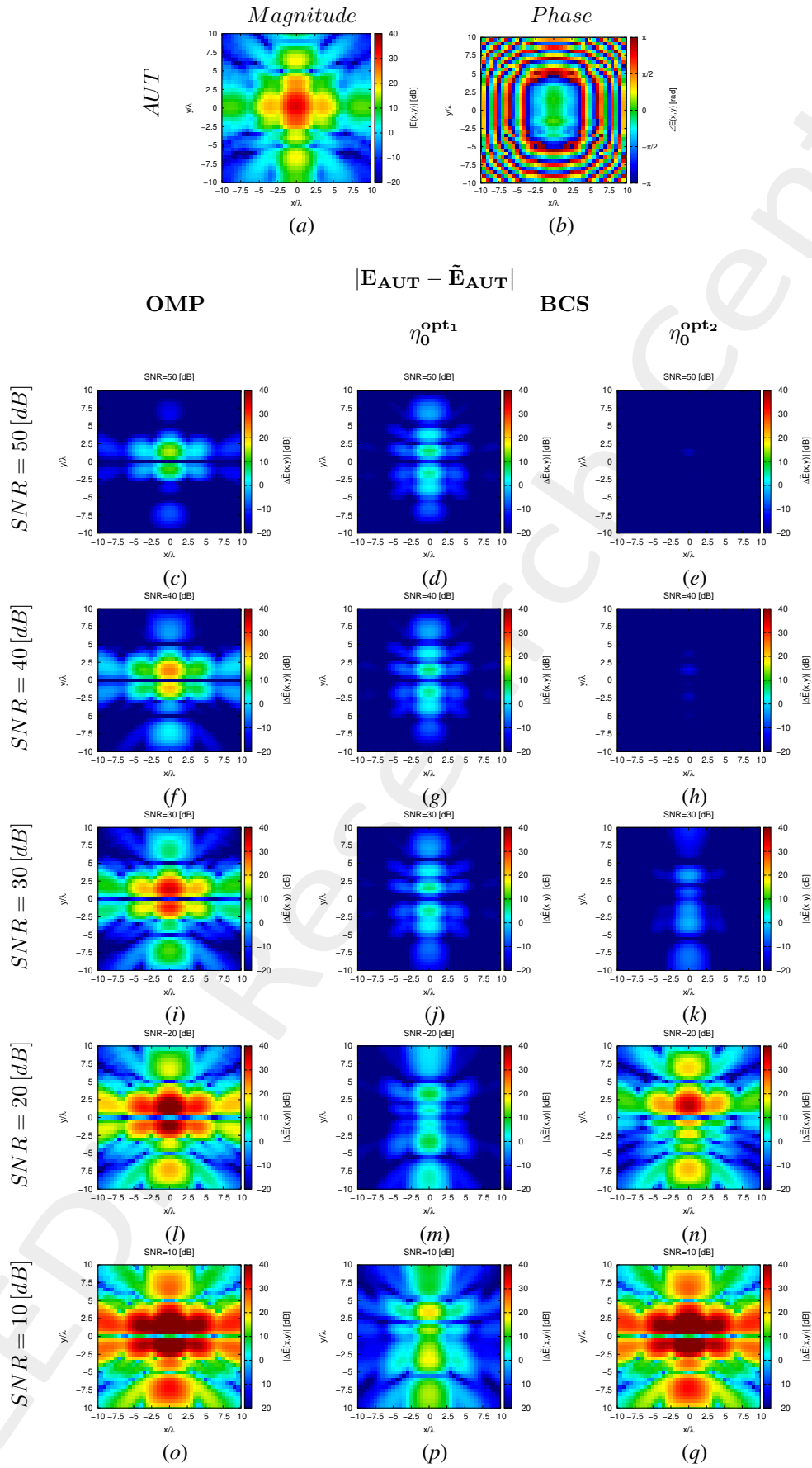


Figure 14: Magnitude difference between the actual and estimated 2 - D near-field pattern when processing noisy measurements at different SNRs.

Estimated Coefficients

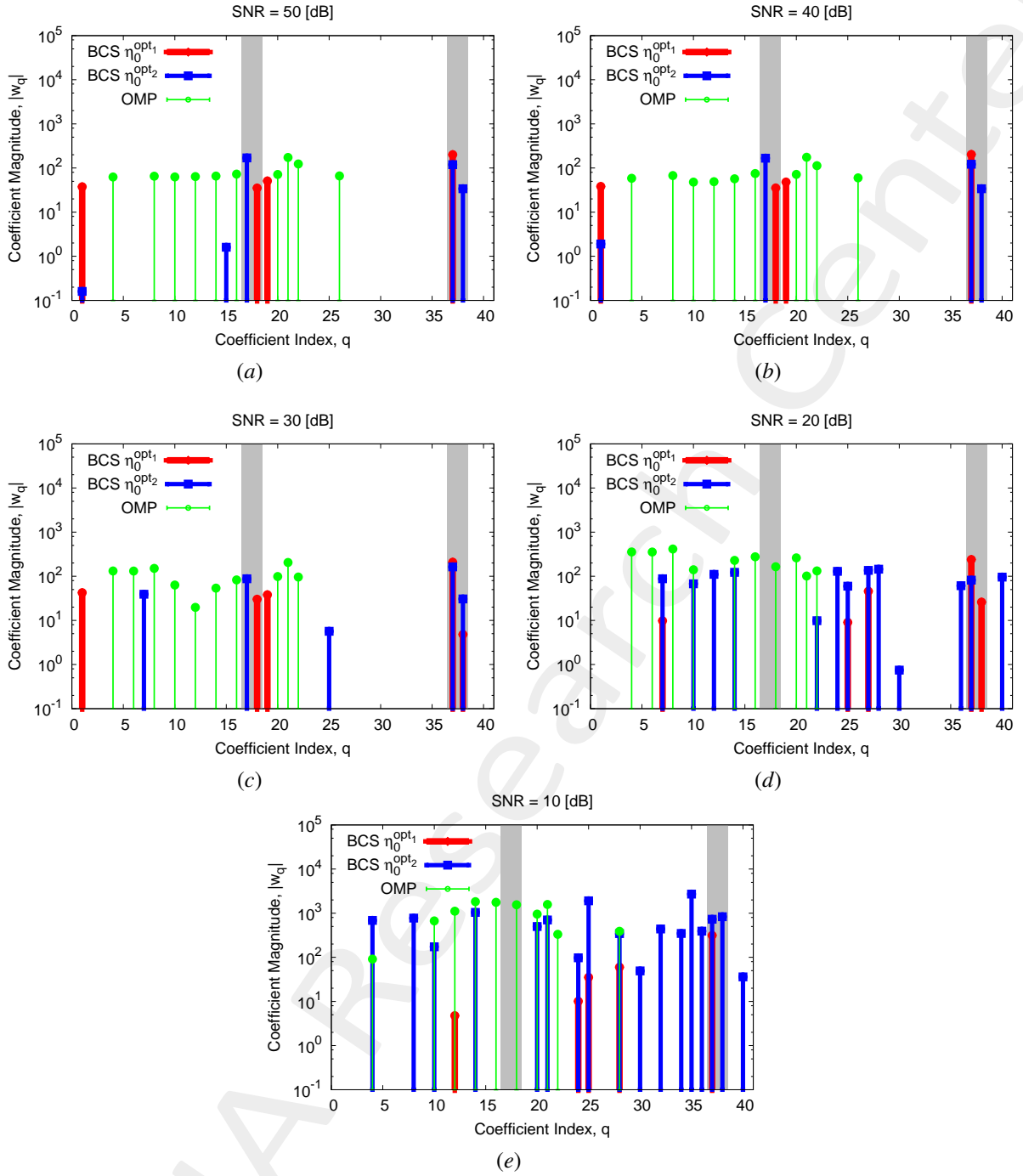


Figure 15: Coefficient comparison between original (*OMP*) and alternative (*BCS*) MbD : (a) $SNR = 50$ [dB], (b) $SNR = 40$ [dB], (c) $SNR = 30$ [dB], (d) $SNR = 20$ [dB], (e) $SNR = 10$ [dB]

Observations

- The *OMP* algorithm is not able to select the vectors concerning the failures affecting the 9th row of the *AUT* for $SNR \geq 20$ [dB] while for $SNR < 20$ [dB] it identifies the magnitude failure. In general, the *OMP* tends to select more vectors associated to magnitude failures rather than those related to phase failures;
- The *BCS* algorithm obtains solutions which are not much sparse when the $SNR = 10$ [dB], in particular when η_0^{opt2} is used, but become sparse for $SNR \geq 30$ [dB]; furthermore, the *BCS* correctly detects both magnitude

and phase failures, at first with low precision (i.e. for $SNR = 30 [dB]$) and then with very high exactness for $SNR \geq 40 [dB]$, independently what value of η_0 is used.

ELEDIA Research Center

1.2.2 OMP vs best BCS

The main idea of this section is to compare the performance of the *OMP* algorithm and the best *BCS* configuration.

Near-Field Error

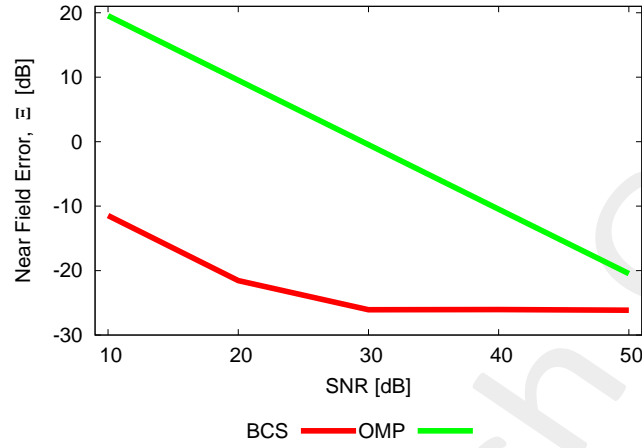


Figure 16: Near Field Error comparison between original (*OMP*) and alternative (*BCS*) MbD for different *SNR* values.

<i>SNR</i> [dB]	Near Field Error, Ξ [dB]	
	<i>BCS</i>	<i>OMP</i>
50	-26.12	-20.47
40	-26.04	-10.47
30	-26.07	-0.47
20	-21.56	9.53
10	-11.46	19.53

Table V: Near Field Errors obtained by the original (*OMP*) and alternative (*BCS*) MbD

Estimated Far-Field

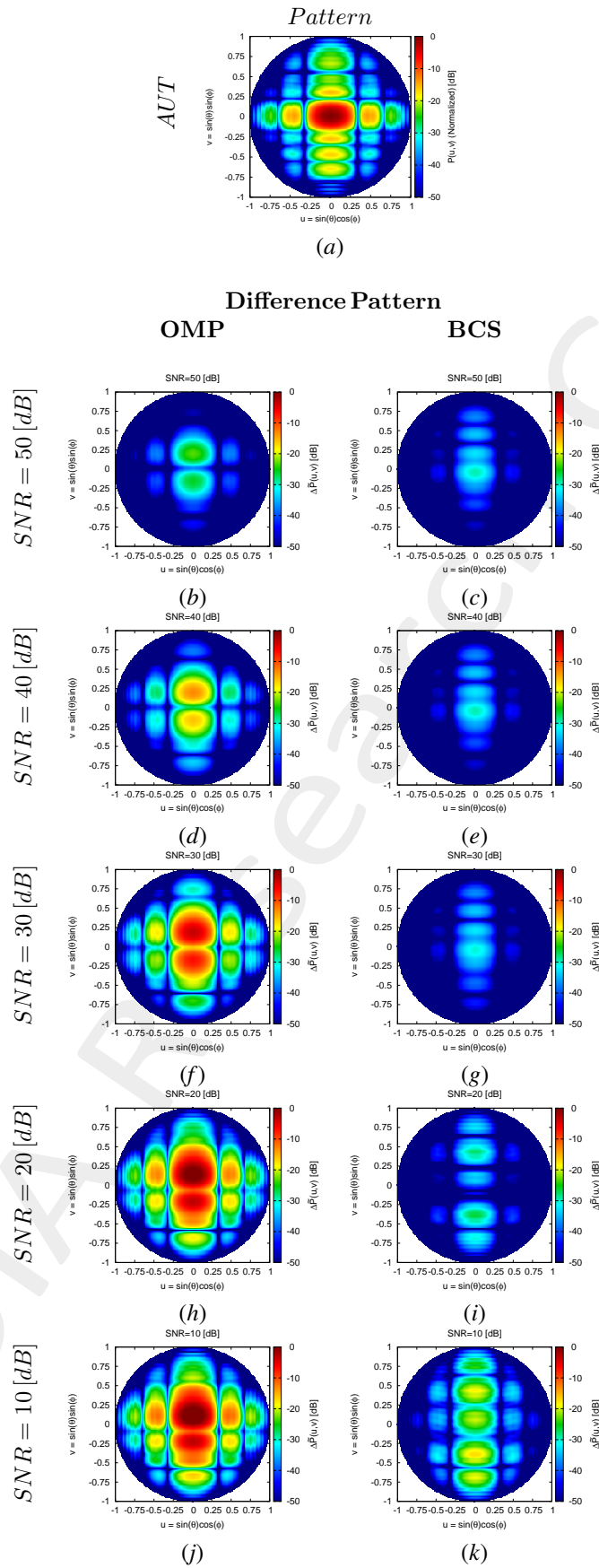


Figure 17: Difference between the actual and estimated 2 – D far-field pattern when processing noisy measurements at different $SNRs$.

Cut @ $v = 0$

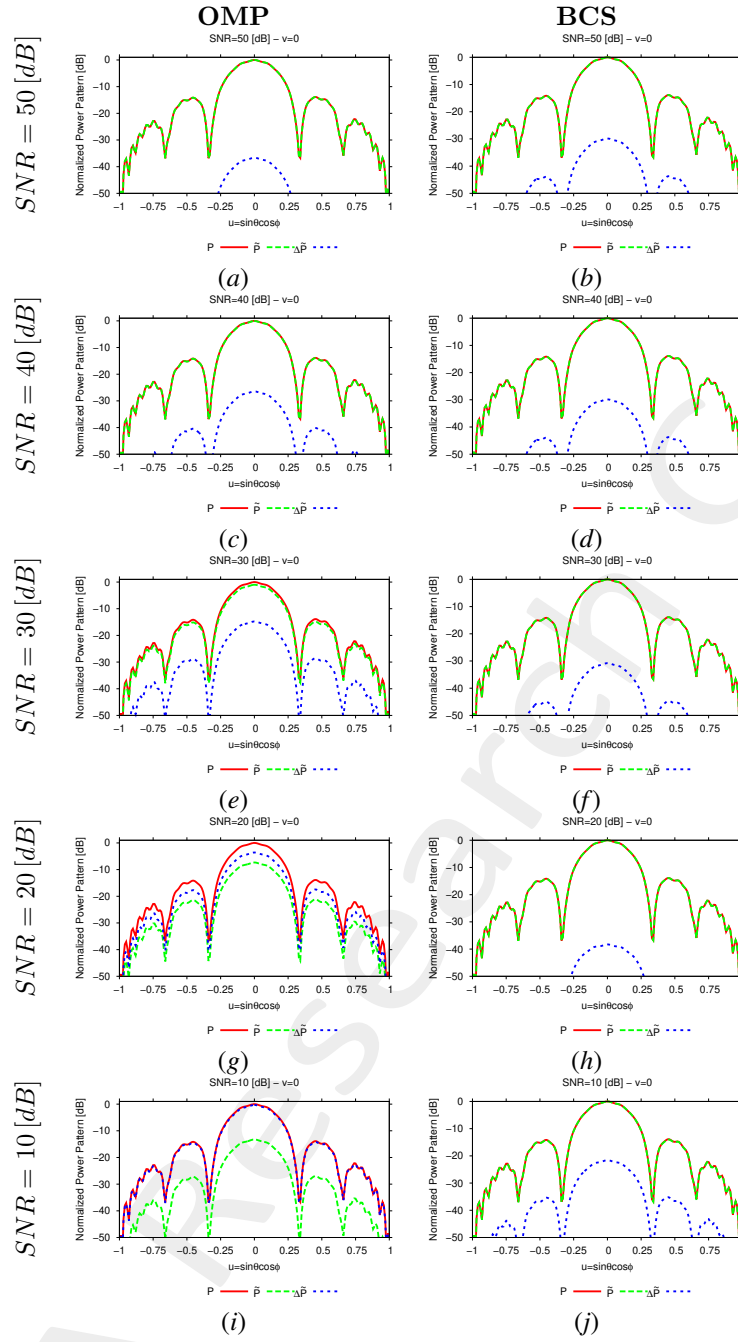


Figure 18: 1 – D cuts of the estimated far-field pattern (obtained through near-to-far-field transformation from the estimated near-field patterns) under several noisy conditions

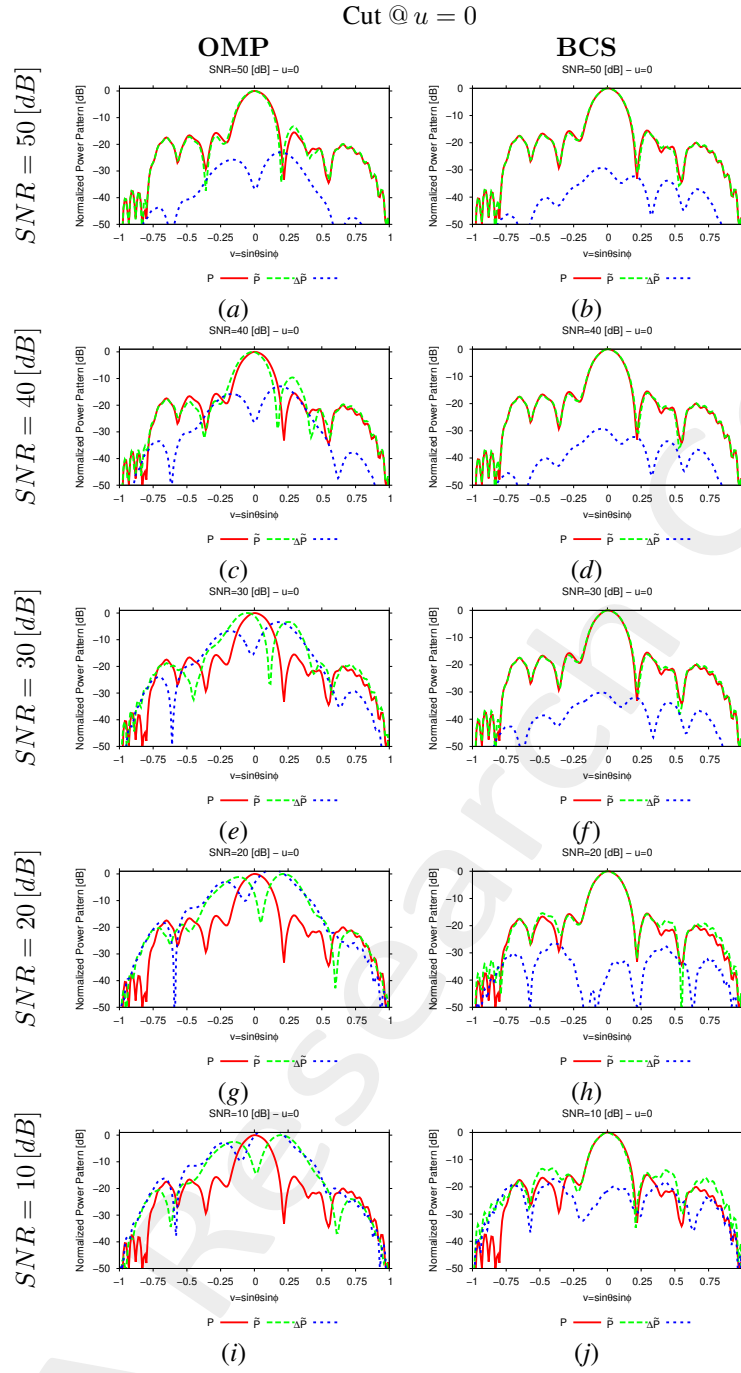


Figure 19: 1 – D cuts of the estimated far-field pattern (obtained through near-to-far-field transformation from the estimated near-field patterns) under several noisy conditions

SNR [dB]	Far – Field Error, χ [dB]	
	BCS	OMP
50	–26.45	–20.61
40	–26.36	–10.55
30	–26.50	–1.08
20	–23.01	3.67
10	–12.86	4.52

Table VI: Far-field matching error between the actual and estimated AUT patterns (both obtained through near-to-far-field transformation from the corresponding near-field patterns) under several noisy conditions.

Estimated Coefficients

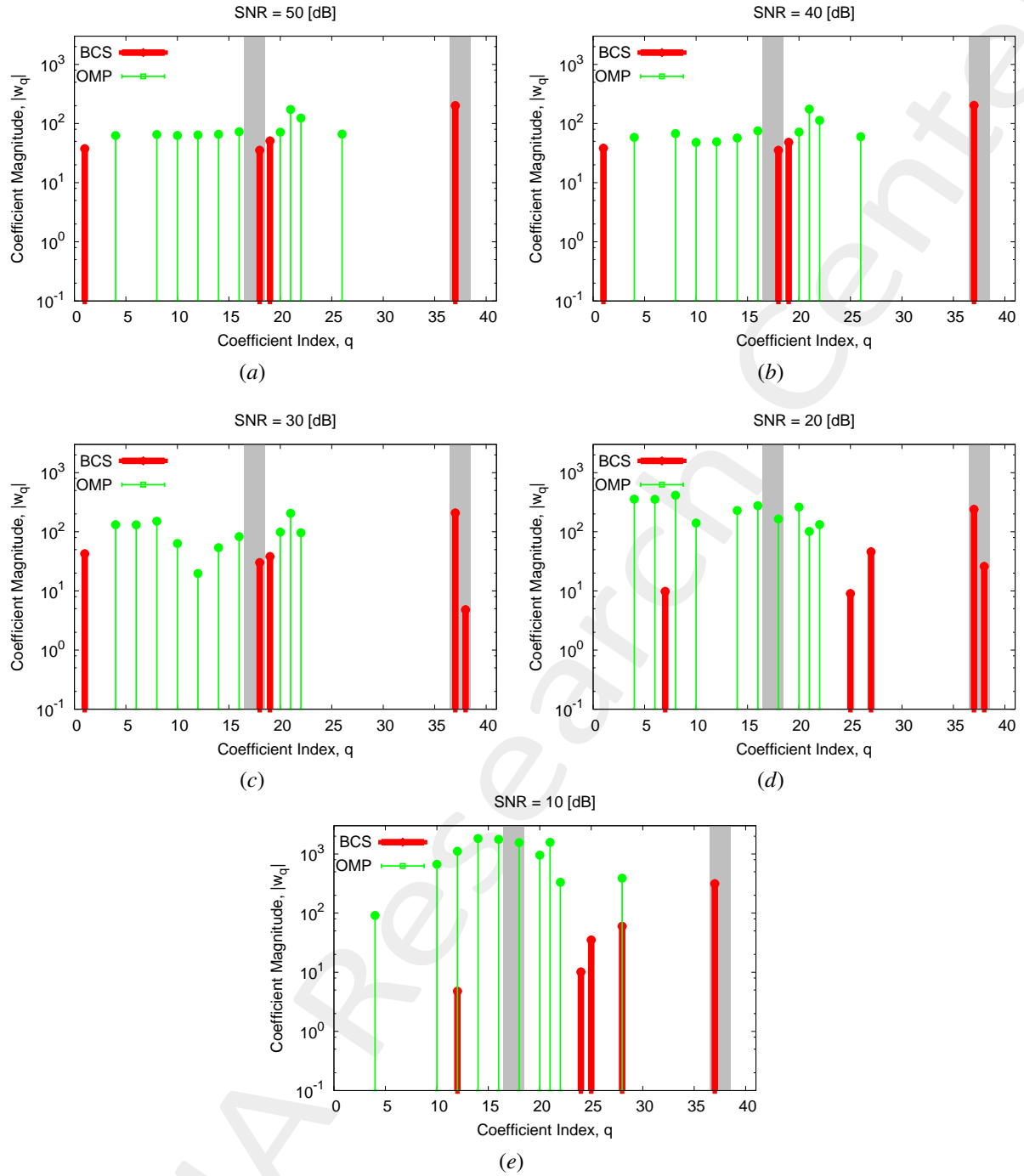


Figure 20: Coefficient comparison between original (*OMP*) and alternative (*BCS*) MbD: (a) $SNR = 50$ [dB], (b) $SNR = 40$ [dB], (c) $SNR = 30$ [dB], (d) $SNR = 20$ [dB], (e) $SNR = 10$ [dB]

More information on the topics of this document can be found in the following list of references.

References

- [1] M. Salucci, N. Anselmi, M. D. Migliore and A. Massa, "A bayesian compressive sensing approach to robust near-field antenna characterization," *IEEE Trans. Antennas Propag.*, vol. 70, no. 9, pp. 8671-8676, Sep. 2022 (DOI: 10.1109/TAP.2022.3177528).
- [2] B. Li, M. Salucci, W. Tang, and P. Rocca, "Reliable field strength prediction through an adaptive total-variation CS technique," *IEEE Antennas Wirel. Propag. Lett.*, vol. 19, no. 9, pp. 1566-1570, Sep. 2020.
- [3] M. Salucci, M. D. Migliore, P. Rocca, A. Polo, and A. Massa, "Reliable antenna measurements in a near-field cylindrical setup with a sparsity promoting approach," *IEEE Trans. Antennas Propag.*, vol. 68, no. 5, pp. 4143-4148, May 2020.
- [4] G. Oliveri, M. Salucci, N. Anselmi, and A. Massa, "Compressive sensing as applied to inverse problems for imaging: theory, applications, current trends, and open challenges," *IEEE Antennas Propag. Mag. - Special Issue on "Electromagnetic Inverse Problems for Sensing and Imaging,"* vol. 59, no. 5, pp. 34-46, Oct. 2017.
- [5] A. Massa, P. Rocca, and G. Oliveri, "Compressive sensing in electromagnetics - A review," *IEEE Antennas Propag. Mag.*, pp. 224-238, vol. 57, no. 1, Feb. 2015.
- [6] A. Massa and F. Teixeira, "Guest-Editorial: Special Cluster on Compressive Sensing as Applied to Electromagnetics," *IEEE Antennas Wirel. Propag. Lett.*, vol. 14, pp. 1022-1026, 2015.
- [7] G. Oliveri, N. Anselmi, M. Salucci, L. Poli, and A. Massa, "Compressive sampling-based scattering data acquisition in microwave imaging," *J. Electromagn. Waves Appl.*, vol. 37, no. 5, pp. 693-729, March 2023 (DOI: 10.1080/09205071.2023.2188263).
- [8] G. Oliveri, L. Poli, N. Anselmi, M. Salucci, and A. Massa, "Compressive sensing-based Born iterative method for tomographic imaging," *IEEE Trans. Microw. Theory Techn.*, vol. 67, no. 5, pp. 1753-1765, May 2019.
- [9] M. Salucci, L. Poli, and G. Oliveri, "Full-vectorial 3D microwave imaging of sparse scatterers through a multi-task Bayesian compressive sensing approach," *J. Imaging*, vol. 5, no. 1, pp. 1-24, Jan. 2019.
- [10] M. Salucci, A. Gelmini, L. Poli, G. Oliveri, and A. Massa, "Progressive compressive sensing for exploiting frequency-diversity in GPR imaging," *J. Electromagn. Waves Appl.*, vol. 32, no. 9, pp. 1164-1193, 2018.
- [11] N. Anselmi, L. Poli, G. Oliveri, and A. Massa, "Iterative multi-resolution bayesian CS for microwave imaging," *IEEE Trans. Antennas Propag.*, vol. 66, no. 7, pp. 3665-3677, Jul. 2018.
- [12] N. Anselmi, G. Oliveri, M. A. Hannan, M. Salucci, and A. Massa, "Color compressive sensing imaging of arbitrary-shaped scatterers," *IEEE Trans. Microw. Theory Techn.*, vol. 65, no. 6, pp. 1986-1999, Jun. 2017.

-
- [13] N. Anselmi, G. Oliveri, M. Salucci, and A. Massa, "Wavelet-based compressive imaging of sparse targets" *IEEE Trans. Antennas Propag.*, vol. 63, no. 11, pp. 4889-4900, Nov. 2015.
- [14] G. Oliveri, P.-P. Ding, and L. Poli, "3D crack detection in anisotropic layered media through a sparseness-regularized solver," *IEEE Antennas Wirel. Propag. Lett.*, vol. 14, pp. 1031-1034, 2015.
- [15] L. Poli, G. Oliveri, P.-P. Ding, T. Moriyama, and A. Massa, "Multifrequency Bayesian compressive sensing methods for microwave imaging," *J. Opt. Soc. Am. A*, vol. 31, no. 11, pp. 2415-2428, 2014.
- [16] G. Oliveri, N. Anselmi, and A. Massa, "Compressive sensing imaging of non-sparse 2D scatterers by a total-variation approach within the Born approximation," *IEEE Trans. Antennas Propag.*, vol. 62, no. 10, pp. 5157-5170, Oct. 2014.
- [17] L. Poli, G. Oliveri, F. Viani, and A. Massa, "MT-BCS-based microwave imaging approach through minimum-norm current expansion," *IEEE Trans. Antennas Propag.*, vol. 61, no. 9, pp. 4722-4732, Sep. 2013.
- [18] F. Viani, L. Poli, G. Oliveri, F. Robol, and A. Massa, "Sparse scatterers imaging through approximated multitask compressive sensing strategies," *Microwave Opt. Technol. Lett.*, vol. 55, no. 7, pp. 1553-1558, Jul. 2013.
- [19] L. Poli, G. Oliveri, P. Rocca, and A. Massa, "Bayesian compressive sensing approaches for the reconstruction of two-dimensional sparse scatterers under TE illumination," *IEEE Trans. Geosci. Remote Sensing*, vol. 51, no. 5, pp. 2920-2936, May 2013.
- [20] P. Rocca, N. Anselmi, M. A. Hannan, and A. Massa, "Conical frustum multi-beam phased arrays for air traffic control radars," *Sensors*, vol. 22, no. 19, 7309, pp. 1-18, 2022 (DOI: 10.3390/s22197309)
- [21] F. Zardi, G. Oliveri, M. Salucci, and A. Massa, "Minimum-complexity failure correction in linear arrays via compressive processing," *IEEE Trans. Antennas Propag.*, vol. 69, no. 8, pp. 4504-4516, Aug. 2021.
- [22] N. Anselmi, G. Gottardi, G. Oliveri, and A. Massa, "A total-variation sparseness-promoting method for the synthesis of contiguously clustered linear architectures," *IEEE Trans. Antennas Propag.*, vol. 67, no. 7, pp. 4589-4601, Jul. 2019.
- [23] M. Salucci, A. Gelmini, G. Oliveri, and A. Massa, "Planar arrays diagnosis by means of an advanced Bayesian compressive processing," *IEEE Trans. Antennas Propag.*, vol. 66, no. 11, pp. 5892-5906, Nov. 2018.
- [24] L. Poli, G. Oliveri, P. Rocca, M. Salucci, and A. Massa, "Long-Distance WPT Unconventional Arrays Synthesis," *J. Electromagn. Waves Appl.*, vol. 31, no. 14, pp. 1399-1420, Jul. 2017.
- [25] G. Oliveri, M. Salucci, and A. Massa, "Synthesis of modular contiguously clustered linear arrays through a sparseness-regularized solver," *IEEE Trans. Antennas Propag.*, vol. 64, no. 10, pp. 4277-4287, Oct. 2016.
- [26] M. Carlin, G. Oliveri, and A. Massa, "Hybrid BCS-deterministic approach for sparse concentric ring isophoric arrays," *IEEE Trans. Antennas Propag.*, vol. 63, no. 1, pp. 378-383, Jan. 2015.
- [27] G. Oliveri, E. T. Bekele, F. Robol, and A. Massa, "Sparsening conformal arrays through a versatile BCS-based method," *IEEE Trans. Antennas Propag.*, vol. 62, no. 4, pp. 1681-1689, Apr. 2014.
-

-
- [28] F. Viani, G. Oliveri, and A. Massa, "Compressive sensing pattern matching techniques for synthesizing planar sparse arrays," *IEEE Trans. Antennas Propag.*, vol. 61, no. 9, pp. 4577-4587, Sept. 2013.
- [29] P. Rocca, M. A. Hannan, M. Salucci, and A. Massa, "Single-snapshot DoA estimation in array antennas with mutual coupling through a multi-scaling BCS strategy," *IEEE Trans. Antennas Propag.*, vol. 65, no. 6, pp. 3203-3213, Jun. 2017.
- [30] M. Carlin, P. Rocca, G. Oliveri, F. Viani, and A. Massa, "Directions-of-arrival estimation through Bayesian Compressive Sensing strategies," *IEEE Trans. Antennas Propag.*, vol. 61, no. 7, pp. 3828-3838, Jul. 2013.
- [31] M. Carlin, P. Rocca, G. Oliveri, and A. Massa, "Bayesian compressive sensing as applied to directions-of-arrival estimation in planar arrays," *J. Electromagn. Waves Appl.*, vol. 2013, pp. 1-12, 2013 (DOI :10.1155/2013/245867).